Published in final edited form as:

IEEE Trans Antennas Propag. 2017 ; 65: . doi:10.1109/TAP.2017.2722876.

Analysis of E-Band Path Loss and Propagation Mechanisms in the Indoor Environment

Jelena Senic,
Communications Technology Laboratory, National Institute of Standards and Technology, Boulder, CO 80305 USA

Camillo Gentile [Member, IEEE],
Communications Technology Laboratory, National Institute of Standards and Technology, Gaithersburg, MD 20899 USA

Peter B. Papazian [Senior Member, IEEE],
Communications Technology Laboratory, National Institute of Standards and Technology, Boulder, CO 80305 USA

Kate A. Remley [Fellow, IEEE], and
Communications Technology Laboratory, National Institute of Standards and Technology, Boulder, CO 80305 USA

Jae-Kark Choi
Tactical Communications Team, Hanwha Systems, Gyeonggi-do 13524, South Korea

Abstract

Millimeter-wave transceivers will feature massive phased-array antennas whose pencilbeams can be steered toward the angle of arrival of the propagation path having the maximum power, exploiting their high gain to compensate for the greater path loss witnessed in the upper spectrum. For this reason, maximum-power path-loss models, in contrast to conventional ones based on the integrated power from an omnidirectional antenna, may be more relevant. Yet to our knowledge, they do not appear in the literature save for one reference. In this paper, we compare both model types at 83.5 GHz for four indoor environments typical of hotspot deployments in line-of-sight (LOS) and non-LOS conditions up to a range of 160 m. To fit the models, we conducted a measurement campaign with over 3000 different transmitter–receiver configurations using a custom-designed channel sounder capable of extracting the delay and 3-D angle of arrival of the received paths with super-resolution. The models are supported by a detailed analysis of the propagation mechanisms of direct transmission, reflection, and knife-edge diffraction to shed light on their interplay in the E-band regime.

Index Terms

Channel propagation modeling; E-band; millimeter-wave wireless (mmWave); mmWave frequencies

Correspondence to: Jelena Senic.

I. Introduction

In july of 2016, the Federal Communications Commission (FCC) issued an unprecedented order for the licensed operation of millimeter-wave (mmWave) bands for terrestrial wireless communications. The new bands are centered at 28, 37, and 39 GHz. In addition, the order extended the unlicensed 60-GHz band from 57–63 GHz to 71 GHz. In total, nearly 11 GHz of spectrum was released. The 95-GHz band is also currently under review [1]. The FCC's decision was prompted by the "spectrum crunch" below 6 GHz, resulting from data-intensive smartphones which have flooded the market over the past decade. Although propagation is less favorable in the mmWave regime, channels with contiguous bandwidths three orders of magnitude wider will enable multi- Gb/s wireless communications [2].

To effectively design the communication systems, fundamental understanding of the propagation characteristics expressed through channel models is required. The most basic and useful model for link-layer analysis is path loss. The choice spectrum allocated by the FCC lies around 30 GHz. A good list of publications for indoor path-loss models; there has already been amassed in the literature. Some of the most recent, which consider obstructed-line-of-sight (OLOS) and non-LOS (NLOS) conditions in the range up to tens of meters, are [3]–[7]. Similar setups can be found at 45 GHz in [8] and at 60 GHz in [9]–[15]. Although 60 GHz is less favorable due to oxygen absorption loss, it is still attractive given the broad unlicensed band. As such, the aforementioned bands have been studied the most.

What has received significantly less attention is the E-band (71–76 GHz, 81–86 GHz, and 92–95 GHz). Even though these bands have licensing requirements and greater penetration loss than 60 GHz, they are not subjected to oxygen absorption. Thanks to new transistor technology, use of these bands for mobile wireless is becoming feasible. However, there is a lack of propagation measurements for this band, both indoors and outdoors. In [16], spatiotemporal models are provided at 72 GHz (and 63 GHz) for an office environment from 24 measurements in LOS conditions up to a range of 10 m. In [17], wideband measurements were taken at 70, 88, and 108 GHz in LOS up to 6 m. Less recently, slightly longer range measurements were taken at 94 GHz in LOS and OLOS conditions [18], [19]. And in [20], path-loss models and dispersion statistics in LOS and NLOS at 73 GHz (and 28 GHz) are provided for an indoor office environment; the models were collected for 48 different transmitter–receiver (TX–RX) configurations in the range 4–46 m. Path-loss models for different indoor and outdoor scenarios in LOS and NLOS up to 100 GHz are presented in [21] and [22].

All of the references save one [20] base their models on the received power measured with an omnidirectional antenna. Conversely, mmWave transceivers will likely feature massive phased-array antennas whose pencilbeams can be steered toward the angle of arrival of the propagation path with maximum power, exploiting their high gain to compensate for the greater path loss witnessed in the upper spectrum. The reason omnidirectional path-loss models are prevalent is because channel estimation to compute the array weights for beamsteering will be carried out with an omnidirectional beam at the lowest bearer (modulation and coding scheme). Once the weights are computed, however, path-loss models for the maximum-power path combined with the directional gain of the beam may be

more relevant to determine the highest bearer attainable and, as such, are also provided in this paper. The models were generated at 83.5 GHz from over 3000 different TX–RX configurations in four environments typical of indoor hotspot deployments, comprising a wide range of wall materials.

Perhaps more valuable than path-loss models is the understanding of how the various propagation mechanisms give rise to multipath, especially since each mechanism will have different scattering properties. In LOS, the direct path will always be accessible and so will dominate; in NLOS conditions, however, as we shall see for the wall materials examined, it suffers from high penetration loss and consequently passes undetected. The general consensus is that diffraction plays a lesser role in the mmWave regime, and that in NLOS, the RX will rely instead on ambient reflected paths [23], [24]. Indeed, through detailed analysis, we quantify how much weaker the diffracted paths can be.

The outline of this paper is as follows. Section II provides an overview of the radio sounder that we designed to collect channel-impulse-response (CIR) data and how it was processed into multipath components (MPCs) and, subsequently, into path-loss data. Section III presents maximum-power and omnidirectional models and how their parameters were fit to data in the four environments. Propagation analysis and discussion on the parameters are reserved for this section as well. The conclusion is drawn in Section IV.

II. Measurement System and Data

In this section, we provide a brief overview of the channel sounder that we designed to conduct the measurement campaigns, in particular how the system records and processes CIRs for the purpose of fitting path-loss models to the collected data.

A. Channel Sounder

A detailed description of our 83.5-GHz channel sounder can be found in [25] and [26]. The system is equipped with a single transmit antenna featuring an omnidirectional pattern in azimuth and a 45° beamwidth in elevation. At the RX is a custom-designed scalar-feed-horn antenna array with 16 elements arranged in the 3-D space. The adjacent elements are spaced 45° apart in both azimuth and elevation, enabling extraction of the 3-D angle of arrival of the received paths. The measured antenna pattern for each element matched the specification patterns provided by the manufacturer to 0.1 dB within the 3-dB beamwidth. The synthesized array pattern of the ensemble of elements [26, Fig. 2] is also omnidirectional in azimuth and has a beamwidth of approximately 90° in elevation with boresight of 22.5°, covering most of the upper hemisphere and some of the lower. This configuration simulated a hotspot setup in which the TX was fixed at 2.5 m in elevation and the RX was lower, at 1.6 m. Because the pattern rolloff is gradual, the RX can actually see a much broader elevation angle than 90°.

The TX sends a pseudorandom sequence with a bit rate of 1 Gb/s occupying a null-to-null bandwidth of 2 GHz. By individually correlating the signal received at each element with the known sequence, 16 different CIRs are generated for a single measurement. Timing and synchronization are maintained with two rubidium clocks, one at the TX and the other at the

RX. They are synchronized with each other using a pulse-per-second direct interface before measurements. After the clocks are synchronized, a start trigger is sent to the RX from the arbitrary waveform generator. This start trigger will synchronize the digitizer trigger and the 4-bit output signal used to switch the multiplexer between array elements. The channel sounder is calibrated through a back-to-back method to compensate for the nonideal system response [26]. Factoring in the TX power, the antenna gains, the noise figure of the RX, and the processing gain of the sequence, the measurable dynamic range of the system is 140.2 dB.

To analyze the measured data, the position, velocity, and heading of the RX array are needed. This information is provided through a robotic mobile positioning system [red box-like apparatus in the foreground of Fig. 1(a)]. The survey area is first mapped through the robot's laser range finder. Once the map is created, the onboard computer can direct the robot to waypoints while simultaneously recording position information from the navigation system and controlling the digitizer. In this way, the information can be queried and stored with the digitizer data at millisecond intervals, while the robot is moving. Internal studies at NIST have shown position errors of 20 cm at 100-m range and angular errors of ~1°. Further details of the channel sounder and mobile positioner are provided in [25].

B. Measurement Data

The system collected measurements in a number of TX–RX configurations throughout each environment. Let i denotes the configuration index and d_i denotes the TX–RX distance reported by the robot. The 16 CIRs from one measurement were synthesized through the space-alternating generalized expectation–maximization (SAGE) algorithm [27]–[29] to yield the directional impulse response of the channel. Specifically, the algorithm extracts the MPCs indexed through j of measured channel i with super-resolution, namely, its complex amplitude (a_{ij}), delay, and angle of arrival (azimuth and elevation). Fig. 2 displays a plot of the MPCs, for example, directional impulse response. (Elevation dimension is omitted to enhance visualization.) Another method [30] to extract multipath used extensively throughout the community offers advantages such as simplicity without any appreciable loss in accuracy.

From the extracted components, two path-loss metrics were computed: one for the maximum-power path $\mathrm{PL}^{\mathrm{BEST}}$ and other for the paths combined from all directions $\mathrm{PL}^{\mathrm{OMNI}}$

$$\mathrm{PL}^{\mathrm{BEST}}(d_i) = -10\log_{10}\max_j |a_{ij}|^2 \quad (1a)$$

$$\mathrm{PL}^{\mathrm{OMNI}}(d_i) = -10\log_{10}\sum_j |a_{ij}|^2. \quad (1b)$$

For each configuration, 32 measurements were collected over a period of 67 ms, while the robot was in motion. Depending on its speed, the robot traveled 20–40 mm, roughly seven to

ten wavelengths. To factor out small-scale fading, the metrics were averaged over the 32 points. Once collected, the robot downloaded the data and then began measuring for the next configuration. The average distance between configurations was about 30 cm.

For the sake of comparison, the free-space (FS) path-loss model given by the Friis transmission equation [31] is also provided here

$$\mathrm{PL}^{\mathrm{FS}}(d_i) = -10\log_{10}\left(\frac{\lambda}{4\pi d_i}\right)^2 \quad (2)$$

where λ is the wavelength of the RF carrier.

The details of the implementation of the SAGE algorithm, including angular resolution and super-resolution techniques employed, have been included in [25] and [26]. Essentially, the measured channel is represented as a superposition of all detected MPCs, each one scaled by a complex amplitude and shifted by the path delay at the RX array center, plus noise. Because we are dealing with real measurements, the reference pulse of the system representing each MPC is required and so is characterized through a back-to-back method. Note that since each array element will have different antenna pattern and positions with respect to the array center, an MPC will appear with different shifts/scales at each element. Hence, indispensable to the algorithm is the element antennas patterns and the precise geometry of the array. Through a greedy version of the expectation–maximization algorithm, SAGE determines the complex amplitude, delay, and angle of arrival (azimuth, elevation) of each MPC—in a collective fashion—that will reconstruct the measured CIRs with minimum error. Note that the MPCs are extracted down to the noise level and so the measured and reconstructed MPCs will have the same power within the error.

The beamwidth of the antennas on the RX array is very large 45°, because we rely on overlap between adjacent array elements so that an impinging MPC can be detected at at least two elements, but typically up to 4 or 5. The different arrival times of the MPC at the individual elements are compared in order to estimate its arrival angle. What is important to understand is that in our system, it is the delay of the system that provides resolution, not the beamwidth of the antennas. The inherent delay resolution of the system is 1 ns (given by the 1-GHz 3-dB bandwidth of the system) so that MPCs 1 foot apart can be resolved. In addition, by employing the super-resolution SAGE algorithm, which considers the complex amplitude of each MPC, the resolution is actually better than this. These topics are all treated in the papers cited.

III. Path-Loss Models

In this section, path-loss models for four environments are presented. The first two environments, the basement and the hallway, are in LOS and so are the simplest to explain while the second two, the lobby/hallway and lobby/conference room, bear NLOS components, warranting more elaborate discussions.

We adopt a generalized breakpoint (BP) model for path loss in dB

$$\mathrm{PL(d)} = \begin{cases} 10\alpha_0 \log_{10}\left(\frac{d}{d_0}\right) + \beta_0 + \mathbb{N}(0,\sigma_0), & d \le d_1 \\ \overline{\mathrm{PL}}(\mathrm{d}_1) + 10\alpha_1 \log_{10}\left(\frac{d}{d_1}\right) + \beta_1 + \mathbb{N}(0,\sigma_1), & d > d_1 . \end{cases} \quad \text{(3a) (3b)}$$

The parameter β_0 denotes the reference loss at $d_0 = 1$ m, while α_0 and σ_0, respectively, denote the loss exponent and standard deviation of the normally distributed shadowing component before the BP distance d_1. The parameters have analogous values (α_1, β_1, σ_1) in the post-BP segment, except for β_1 which is the step loss, i.e., the transitional loss in excess of the average loss at the breakpoint. The average loss $\overline{\mathrm{PL}}(\mathrm{d}_1)$ is defined as

$$\overline{\mathrm{PL}}(\mathrm{d}_1) = 10\,\alpha_0 \log_{10}\left(\frac{d_1}{d_0}\right) + \beta_0 . \quad (4)$$

Because the path-loss model is only a function of the distance between the TX and RX, the model is independent of specific TX–RX locations, i.e., wide-sense stationary [32]. Accordingly, measurements should be taken over an ensemble of many TX–RX configurations to abstract out the site-specific characteristics [20].When this is done, the existence of a BP to date is controversial: raytracing simulations in [33] showed that a BP might exist; however, extensive measurements in the same paper showed no BP; similarly, in [34], raytracing predicted a BP to exist in a microcell outdoor urban environment at large distances, while measurements in the same paper showed no BP in the same measured environment.

Abstracting out the site-specific characteristics will of course lead to a larger standard deviation—oftentimes much larger—than what would otherwise be witnessed at any single TX location. In addition, it has been observed that stationarity may not apply to the mmWave systems [35]. Finally, since link distances will be much shorter than for sub 6-GHz, path loss will be more localized to the TX. Consequently, in our work, we present site-specific models. A BP was employed wherever a discontinuity in the data points gathered in a single environment was apparent. Such a discontinuity usually reflects a transition from LOS to NLOS, but an exception is noted in the Hallway. Details are given in the following sections.

A. Basement

The first environment considered was the basement[1] area shown in Fig. 1(a). The floor of this area is a metal ground plane, and the walls of the room are cinderblock. The room

[1]The area is actually a laboratory, but since the walls are cinderblock and there are no windows, it is representative of a basement.

ceiling is 4.9 m high. The photograph shows the TX mounted on a tripod (background left) and the RX array mounted on the robot (foreground middle).

Fig. 1(b) illustrates the BEST path-loss model for the Basement as a blue line. It was obtained by fitting (3a) to the $\mathrm{PL}^{\mathrm{BEST}}(d_i)$ data (blue circles) in (1a) through a least-squares regression. Because all measurements were in LOS and the range was so small (less than 7 m), no BP was necessary. Also shown in the plot is the FS model in the red line. The match to the FS is good, both in terms of $\alpha_0^{\mathrm{BEST}} = 1.97 (\alpha^{\mathrm{FS}} = 2.0)$ and $\beta_0^{\mathrm{BEST}} = 71.18\,\mathrm{dB}\ (\beta^{\mathrm{FS}} = 70.85\,\mathrm{dB})$. The nominal TX/RX antenna patterns from the manufacturer were used in the SAGE algorithm (Section II-B) since the antennas have not yet been calibrated in a NIST anechoic chamber. The specifications list the maximum tolerance in the patterns as 2 dB. We attribute any deviations of the data points from the FS line to this tolerance.

The OMNI path-loss model (green line) was similarly obtained from the $\mathrm{PL}^{\mathrm{OMNI}}(d_i)$ data (green pluses) in (1b) instead. Notice that the difference between BEST and OMNI is about 1.4 dB; this means that the maximum path accounts for 72% of the total power and conversely that the secondary paths account for only 28% of it. Furthermore, because each data point in OMNI also incorporates many other secondary arrivals—not just a single arrival—the fluctuations in the individual arrivals average each other out. For this reason, OMNI exhibits a smaller standard deviation ($\sigma_0^{\mathrm{OMNI}} = 0.86\,\mathrm{dB}$) when compared to BEST ($\sigma_0^{\mathrm{BEST}} = 1.09\,\mathrm{dB}$) in this environment and, as we shall see, throughout all four environments for the most part. Table I shows the settings and path-loss model parameters for the environments studied.

B. Hallway

In the Hallway environment, the TX was positioned at a single location, while the robot moved from a range of 6–159 m at the end of the hallway. The ceiling height of the hallway is 7 m and its width is 3.5 m. The path-loss model for this environment can be visualized in Fig. 3. Although LOS was maintained throughout the whole robot trajectory, a discontinuity in the data points is apparent. Further inspection revealed the presence of a staircase there. Accordingly, we implemented the BP model with the BP set to the beginning of the staircase at $d_1 = 26.31$ m. In order to extract the model parameters, the set $(\alpha_0, \beta_0, \sigma_0)$ was first fit to the pre-BP segment of data ($d \leq d_1$) through (3a). In turn, $\overline{\mathrm{PL}}(\mathrm{d}_1)$, was computed from (4). Finally, by rearranging (3b), the set $(\alpha_1, \beta_1, \sigma_1)$ was fit to the difference

$$\mathrm{PL(d)} - \overline{\mathrm{PL}}(\mathrm{d}_1) = 10\alpha_1 \log_{10}\left(\frac{d}{d_1}\right) + \beta_1 + \mathbb{N}(0, \sigma_1), \quad d > d_1 \qquad (5)$$

given $\overline{\mathrm{PL}}(\mathrm{d}_1)$ and the post-BP segment of data ($d > d_1$). The complete set of extracted parameters can be found in Table I.

Although our system has 1-ns resolution capability, because the multipath scattering created by the staircase—an intricate, metallic object—was so rich, with rapidly arriving successive paths, the system could not resolve them. The reflected and diffracted paths then appeared combined with the direct path, for the most part in a constructive sense. That is why the BEST path loss witnessed is actually lower than FS for most points beyond the staircase: the exponents are $\alpha_1^{\mathrm{BEST}} = 1.51$ and $\alpha_1^{\mathrm{OMNI}} = 1.31$ and the step losses, $\beta_1^{\mathrm{BEST}} = -0.99$ and $\beta_1^{\mathrm{OMNI}} = -0.47$, are negative, albeit small, which means that the transition between the zones was smooth.

Notice that the standard deviation of BEST increases from $\sigma_0^{\mathrm{BEST}} = 0.71\,\mathrm{dB}$ to $\sigma_1^{\mathrm{BEST}} = 2.81\,\mathrm{dB}$. The increase is not due to the fluctuation in the power of the direct path but rather to the interference with it by the scattered paths. Notwithstanding, σ_1^{BEST} is still relatively small considering the long range of the measurements. This can be attributed to the stability brought to bear by the direct path. This stability carries over to the OMNI model for which $\sigma_1^{\mathrm{OMNI}} = 1.92\,\mathrm{dB}$.

In contrast to the basement environment, the gap between BEST and OMNI in the hallway widens even in the first segment, from 1.2 dB at the shortest range to 2.4 dB at the BP (secondary power increases, respectively, from 24% to 42% of total power). This is because the LOS segment is much longer here and so more variation throughout is expected. Since the propagation mechanism of the dominant path remains direct transmission throughout the hallway, the secondary power exceeds the dominant power as a percentage of the total—this occurs when the gap is 3 dB—only after 72 m, much beyond the BP. The gap continues to increase, but very slowly, up to 3.6 dB. (Secondary power is 56% of total power.) Note that at the end of the hallway, the signal is still above the 128-dB system noise floor.

C. Lobby/Hallway

In this environment, the TX was placed at five different locations in a lobby area open to the same hallway as in the previous section. The ceiling height of the lobby is 3 m. In the photograph in Fig. 4(a), TX1 stands to the far left as the robot approaches the corner in the hallway. Locations TX1–TX5 and the corner C are shown on the floorplan in Fig. 4(b). The grid spacing is 1 m, and the orientation for the RX angle of arrival is illustrated. For each location, the robot traversed the same trajectory delineated by the black waypoints on the floorplan. For TX1, the LOS trajectory appears as a solid orange line and the NLOS as a dashed-dotted purple line; NLOS conditions were created at BP by the interfering walls as the RX moved down the hallway. Point BP was computed analytically as the intersection of the line (blue dot) containing TX1 and C and the line along the robot's trajectory in the hallway. The BP distance d_1 is given as the distance from TX1 to BP. Note that each TX has a distinct BP.

1) Analysis of Propagation Mechanisms—For accurate path-loss modeling in mm Wave communication systems, a clear understanding of how direct transmission, specular reflection, and knife-edge diffraction interrelate in this frequency regime is essential. The

diversity in the TX locations, as well as the availability of both LOS and NLOS conditions, allows for a much deeper level of analysis here compared to the other environments. First, we analyzed data points for three RX positions around the BP corresponding to a single TX, TX4: positions RX1, RX2, and RX3 are marked in Fig. 5(a). The direct path from TX4 is shown as a dotted blue line, the diffracted paths from the corner as dashed green lines, and the reflected paths from the right side of the hallway as solid red lines.

Analysis involved the visual inspection of the data-derived directional CIR in comparison with simple raytracing predictions. First consider RX1, the position right before the BP, whose directional response is shown in Fig. 5(b). The direct path is apparent in the response due to its first arrival at 41 ns; also because it bears the smallest path loss of all MPCs 90.6 dB. The diffraction path from the corner could not be resolved from the direct path due to the 1-ns resolution of the system. (The two paths theoretically arrived within 0.3 ns of each other.) Diffuse components from the corner at lower power levels are also present along the same angle of arrival. Arriving at 48 ns, later than the direct path due to the longer propagation length, is the reflected path with PL = 107 dB from the right side of the hallway at 319.5°, plus ensuing diffuse components. This is also indicated in Fig. 5(b).

Now consider the directional response of RX2, the position right after the BP, in Fig. 5(c). The direct path was no longer detected due to the high penetration loss of the interfering walls. Instead, the diffracted path at 47.8 ns with PL = 121.2 dB was the first arrival. The reflected path from the right sidewall of hallway was still detected, however with a slightly longer delay (53.9 ns) and a slightly smaller angle (312°) compared to RX1. The reflected path showed PL = 98.9 dB, 22.3 dB less than the diffracted path.

Finally, Fig. 5(d) shows the directional response of RX3 further down the hallway, 4 m from the BP. Here, as with the direct path, the diffracted path has also fallen below the noise floor of the RX and the only dominant path observed was the reflected one at 61.1 ns and 315° with PL = 96 dB.

The estimated path loss, delay, and angle of arrival (AoA) of the dominant paths for TX4 are summarized in Table II. The propagation mechanisms witnessed at the three RX positions for TX4 were similarly witnessed for the other four TXs. To demonstrate this, let us focus on a single RX position (for the sake of brevity). We choose the position right after the BP, the most informative since both the reflected and diffracted paths were detected there: Table III lists their estimated path loss, delay, and AoA for the five TXs. Notice the diffracted paths are significantly weaker (11–22.7 dB) than the reflected paths. This has also been confirmed in [23]. Taken together, these observations suggest that the BEST model represents direct transmission in LOS and for NLOS it represents reflection.

In the raytracing effort, the path loss of the direct path and that of the reflected paths were predicted through (2) as $PL^{FS}(l)$, where l denotes the path length. For the direct path, the equation given $l = d$ is accurate since the path length corresponds to the TX–RX distance. For the reflected path, l is the length of the specular path; here the equation, however, does not account for the reflection loss; hence, the difference between the estimated and predicted values can be viewed as the reflection loss. For the fixed transmitter TX4, the reflection

losses for RX1, RX2, and RX3 are reported in Table II. As illustrated in Fig. 5(a), the three reflections were incident on different wall materials, namely, wooden panels which had the highest loss (12.9 dB), metal-framed glass which had much lower (3.9 dB), and ceramic tiles having close to no loss. Now for the fixed RX position just after the BP, the reflection losses for TX1, TX2, and TX3 were 10.1, 12.7, and 7.6 dB, respectively (see Table III). For these three TXs, the incident signals all encountered the same wooden panels and so we see a comparable range of reflection-loss values; for TX4 and TX5, on the other hand, the signals were incident on the metal-framed glass panes with reflection losses 3.9 and 2.8 dB, also close.

For a more comprehensive comparison with the literature, Langen *et al.* [36] furnish reflection losses at 60 GHz for a host of materials. The losses for wood fell in the range 9.5–11.7 dB versus our observed range 7.6–12.9 dB, 2.9–3.8 dB for glass versus our 2.8–4 dB, and 3.8–5.8 dB for tiles versus our 0–2.7 dB. While the matchup is good, discrepancies do arise from the difference in center frequency and exact wall materials.

Diffraction loss from the corner was predicted through simple knife-edge equations [32]. First, the Fresnel–Kirchoff diffraction parameter ν was calculated. Parameter ν maps to the diffraction gain (G_D) through the formulas provided by Lee [37]. The gain was then subtracted from the FS loss $\mathrm{PL}^{\mathrm{FS}}(d)$ in (2), yielding the predicted path loss of the diffracted path. We see in Table III that the estimated and predicted values agree well with a mean absolute error of 2.18 dB across the five TXs. The mean falls within the same range as the LOS path-loss errors for the Basement in Section III-A. Those errors were attributed to the uncertainty in the TX antenna pattern. In general, errors will arise not only from the measurement system but also in the predicted values due to the inaccuracies in the floorplan. Nevertheless, the mean absolute error in delay across all entries in Table III was only 0.38 ns and 2.50° for the AoA. This suggests that the propagation mechanisms can accurately be predicted through raytracing if the environment is characterized sufficiently well.

2) Transmitter-Specific Path-Loss Models—The remainder of Section III-C is dedicated to path-loss models developed in light of the observations from Section III-C1. We first consider models specific to the TX locations. The BP served to partition the collected data into LOS and NLOS points. Table I shows the fit parameter values for the five TX locations. For the post-BP segment in this environment, a *piecewise* distance $d = d_1 + \Delta d$ was used instead, where Δd denotes the *incremental* distance along the hallway [see Fig. 4(b)]. The piecewise distance provided a least-squares error smaller than the Euclidean distance. This is also supported by evidence in [35] and [38]. The better fit stems from the fact that in NLOS, the main propagation mechanism is reflection along the hallway, not direct transmission through the walls.

To substantiate this further, we examine the BEST model, which represents the main propagation mechanism, versus the Euclidean, piecewise, and incremental distance metrics. We concentrate on the RX location farthest from the TXs, i.e., the NLOS waypoint at the end of the hallway, where the three metrics differ the most. The three are reported in Table IV alongside the average value of the model at the waypoint $\overline{PL}^{\mathrm{BEST}}$ for the five TXs. It is meaningful to compute Pearson's correlation coefficient across the five TXs between the

individual distance metrics (converted to dB scale) and the path loss, as it is expected that path loss increases as the TX gets farther away. Rather for the Euclidean distance, the coefficient is −0.49: the absolute value of the coefficient demonstrates poor correlation and the negative sign demonstrates that the path loss actually decreases instead. The coefficient for the piecewise distance improves to 0.01 (in the sense that the value is nonnegative) albeit the correlation is still poor in absolute value. In contrast, the coefficient for the incremental distance is 0.95: both high correlation and positive sign, as expected. The reason that the latter provides the best correlation is because the majority of the path loss occurs during the NLOS portion and so the incremental distance is the best indicator of this. The preceding remains a purely illustrative exercise since applying the incremental distance (instead of the Euclidean or piecewise distance) has no physical meaning because it is undefined before the BP.

Bear in mind that it is not only the incremental distance that indicates the length of the reflected path in NLOS, but also the incident angle that the specular reflections form with the sides of the hallway. For instance, given the position of TX2, the incident angle is the widest compared to all other TXs. Hence for a fixed incremental distance, the signal necessitates the greatest number of reflections to reach the NLOS waypoint, increasing both the additive reflection loss and the FS loss due to the longer path length. This is another reason why TX2 suffers from the greatest path loss. On the contrary, the narrowest incident angles trace back to TX4 and TX5. Hence, these TXs necessitate the least number of reflections to reach the waypoint, another reason why their losses are the least.

3) Floating-Breakpoint Path-Loss Models—A floating BP model—floating because it is independent of the actual TX BPs in the measurement campaign—is also proposed for lobby/hallway. The model was generated by combining the data from the five TX locations. Specifically, the LOS data from TX1 to TX5 were merged from which a unique set of parameters, (α_0, β_0, σ_0), was extracted through (3a). The set was then used to calculate $\overline{\mathrm{PL}}(\mathrm{d}_1)$ from (4). Note that because each TX has a distinct d_1, each in turn has a distinct $\overline{\mathrm{PL}}(\mathrm{d}_1)$. Next, from the NLOS data for each TX location, the associated $\overline{\mathrm{PL}}(\mathrm{d}_1)$ was subtracted as in (5). The resultant differences from the five locations were merged and a unique set of parameters, (α_1, β_1, σ_1), fit.

The floating model is not more general than the TX-specific models only because it is derived from multiple TX locations, but also because the BP can fall anywhere in the LOS region, not necessarily at the end. This is often the case in practice, e.g., the LOS distance from TX2 to the waypoint at the beginning of the hallway is longer than the minimum NLOS distance for TX2, i.e., the BP distance. The model parameters also appear in Table I and a plot in Fig. 4(c). An indicator variable d_1 = 10 m was chosen deliberately to create overlap between the LOS and NLOS ranges.

In LOS conditions, the extracted parameters match well to FS and the difference between BEST and OMNI is about 0.8 dB, which means that the secondary power is only about 17% of the total power as opposed to 28% in the Basement. The reason for this is twofold: 1) the wall material is less reflective than in the basement; hence, there is more loss per reflection

and 2) the space is larger than in the lab; hence, reflected paths have to travel farther to reach the RX, diminishing their strength.

In NLOS, the step losses, $\beta_1^{\mathrm{BEST}} = 5.54\,\mathrm{dB}$ and $\beta_1^{\mathrm{OMNI}} = 5.64\,\mathrm{dB}$, quantify the drop in power associated with the blockage of the direct path. Here, the dominant propagation mechanism is no longer direct transmission, but reflection instead. This is why the exponent and the standard deviation both increase precipitously from $\alpha_0^{\mathrm{BEST}} = 1.93$ to $\alpha_1^{\mathrm{BEST}} = 6.19$ and from $\sigma_0^{\mathrm{BEST}} = 1.52\,\mathrm{dB}$ to $\sigma_1^{\mathrm{BEST}} = 5.82\,\mathrm{dB}$. Although they experience the same propagation mechanisms here, the exponent of OMNI is smaller than that of BEST, which means that the dominant path dies down at a faster rate than the secondary paths. As a consequence of the different exponents, the gap between BEST and OMNI begins to widen at the BP and ultimately reaches 7.1 dB. At this endpoint, the secondary power accounts for about 81% of the total power.

It is a worthwhile exercise to compare our results with the 73 GHz indoor path-loss models provided in [20] (for V–V antenna polarization). For their directional floating-intercept model [20, Table 7], the loss exponent in LOS is 0.7 and the standard deviation is 2.3 dB. The analogous parameters for our floating-BP BEST model are 1.93 and 1.52 dB, respectively. In NLOS, their BEST model reports a much smaller exponent of 2.9 versus 6.19 in our study, while their 11.7-dB standard deviation is much higher than our 5.82 dB. The smaller exponent might be explained by the fact their NLOS environment is characterized by soft partitions such as cubicles and their walls are made from drywall; our walls, rather, are made from less penetrable stone. The greater diversity in their environment —including desks, chairs, offices, and classrooms, all absent from our environment— also justifies the larger standard deviation. Although it is true that the measurements were taken in different buildings and at offset center frequencies, the stark contrast between the parameters may also arise from the nonuniform modeling approaches, specifically in the number of data points collected, their single-slope model versus our dual-slope model, and their Euclidean distance versus our piecewise distance. This exercise underscores the need for recommended modeling practices in order to facilitate a meaningful comparison between studies. This is one of the goals of the 5G mmWave Channel Model Alliance [39].

D. Lobby/Conference Room

The photograph of the fourth environment is displayed in Fig. 6(a) and the corresponding floorplan in Fig. 6(b). The TX was placed at a single location, TX6, shown in the lobby, while the robot moved along the trajectory within the adjacent conference room (dashed-dotted purple line), amidst tables and chairs in the surroundings. The height of the ceiling is 3 m.

1) Open Doors—We first consider the case for which all three sets of entrance doors to the conference room were open. The location of the TX was chosen deliberately to highlight various propagation mechanisms that are in effect throughout the room. Consider that the BEST data points are shown in Fig. 6(c). Some points are clustered and we denote those clusters as Zones I–IV. They are circled in magenta and labeled accordingly. For these

points, we can infer whether a MPC originated from transmission, reflection, or diffraction, as was done for the lobby/hallway, by comparing the directional CIR to raytracing predictions. The zones are labeled in Fig. 6(a) and (b) as well. A single starred data point in each zone was selected for illustration [see Fig. 6(c)] and the propagation mechanism identified for each zone is depicted in Fig. 6(b).

In Zone I, the RX was in the only LOS area accessible on the trajectory, directly in front of Door A. In Zone II, at the far left of the room, the RX was also apparently in LOS conditions. Further examination, however, revealed that due to the height of the TX the panel above the door in fact blocked the direct path. For Zone II, the dominant mechanism, rather, was diffraction off the lower edge of the panel into the RX. Diffraction is also witnessed in Zone III, off the edges of the two doorways. Although this diffraction is witnessed in two disjoint areas, due to the symmetrical geometry with respect to TX6, it occurs at the same distance in Fig. 6(b). Finally, reflection from the side of Doorway B gave rise to Zone IV, resulting in a reflection loss of 6.8 dB, in line with values reported in Section III-C. Table V shows that the estimated and predicted path loss, delay, and azimuthal angle of arrival agree well at the starred points in each one of the zones.

Reflections from the inner walls, floor, and ceiling of the room are the dominant mechanism for the unclustered BEST points in NLOS conditions. A single-slope path-loss model was fit to them as well as to the analogous OMNI points (omitted in Fig. 6(c) to avoid clutter). Table I contains the fitted parameters. Due to an insufficient number and distance spread of the data points in LOS (Zone I) to guarantee confidence in the fit, the (α_0, β_0, σ_0) parameters were omitted from the table. As such, β_1^{BEST} and β_1^{OMNI} were measured in reference to the FS value at the BP instead. Given the similarities of this environment to lobby/hallway—the first segment is in LOS and then the TX is shadowed by walls—the incremental distance $d = d_1 + \Delta d$ was employed here as well, where d_1 is shown in Fig. 6(b). In fact, note values of $\alpha_1^{\mathrm{BEST}} = 5.75$ and $\alpha_1^{\mathrm{OMNI}} = 3.63$ are comparable, albeit slightly lower, to the floating-BP model in the lobby/hallway, while values of $\beta_1^{\mathrm{BEST}} = 10.54\,\mathrm{dB}$ and $\beta_1^{\mathrm{OMNI}} = 10.10\,\mathrm{dB}$ were closer to the TX2 and TX3 models.

Diffraction plays a lesser role in the mmWave regime and in NLOS the RX will rely mostly on reflected paths. As we showed in the lobby/hallway environment, reflection from the right side of the hallway provided a strong signal at the RX (depending on the wall material), while diffraction was much lower and could not be detected just a few meters away from the corner. It is important to keep in mind that we presented a complex environment—lobby/conference room with open doors and the TX outside—where we showed that when the direct and reflected paths are very weak, diffraction is the dominant mechanism and will cause discontinuity of the path loss data points. Accordingly, our approach was to eliminate the outlying path loss values in the zones and fit without them.

2) Closed Doors—In the second case, considered in this environment, the three wooden entrance doors to the conference room, each with 4.5 cm thickness, were closed, creating NLOS conditions for all RX positions inside. Fig. 6(d) shows the BEST and OMNI data.

Both models are characterized by a steep ascent from the shortest measured range of 6.9 m, when the robot was directly in front of the door, to the same BP $d_1 = 7.3$ m as with open doors, when the robot was completely displaced from the door. As with the open doors, the parameters (α_0, β_0, σ_0) were omitted from Table I due to an insufficient number and distance spread of the pre- BP data. In the post-BP segment, the path loss increases to 121.7 dB for BEST and 114 dB for OMNI ($\beta_1^{\text{BEST}} = 33.6\,\text{dB}$ and $\beta_1^{\text{OMNI}} = 25.9\,\text{dB}$ from the FS baseline, respectively) at the BP, substantial amounts for such a short range. While indeed substantial, the losses remained relatively constant throughout the room as indicated by the exponents $\alpha_1^{\text{BEST}} = 0$ and $\alpha_1^{\text{OMNI}} = 0.04$ and the small standard deviations $\sigma_1^{\text{BEST}} = 2.21\,\text{dB}$ and $\sigma_1^{\text{OMNI}} = 1.43\,\text{dB}$. In the conclusion, so long as the signal could penetrate the room through the doors, it remained at the same power level throughout the room, reaching the RX along various propagation paths.

IV. Conclusion

In this paper, we presented omnidirectional and maximum-power path-loss models for indoor environments at 83.5 GHz. The latter are particularly relevant because mm Wave RXs will steer their pencilbeam antennas toward the direction of the arrival path that has maximum power. The maximum power path-loss model also provides an understanding of the signal propagation and, as such, we hope can contribute to a more efficient design of future 5G systems. The environments investigated are typical of indoor hotspot deployments, namely, a basement, lobby, hallway, and conference room. To fit the models, measurements were recorded from over 3000 different TX–RX configurations in LOS and NLOS conditions up to a range of 160 m.

In addition to path-loss models, we analyzed the propagation mechanisms of direct transmission, specular reflection, and knife-edge diffraction in the environments. This was accomplished through inspection of measured directional channel responses in comparison with raytracing predictions. In NLOS, the direct path was undetected due to high penetration loss; while diffracted paths were detected, their power was recorded 11–23 dB weaker than reflected paths.

Acknowledgments

The authors would like to thank Y. Lo for his support during the measurements campaign.

References

1. Report and Order and Further Notice of Proposed Rulemaking. Federal Communication Commission; Jul, 2016 document FCC-16-89
2. White Paper. Cisco; San Jose, CA, USA: Feb, 2017. Cisco visual networking index: Global mobile data traffic forecast update, 2016–2021. [Online]. Available: http://www.cisco.com/c/en/us/solutions/collateral/service-provider/visual-networking-index-vni/mobile-whitepaper-c11-520862.pdf
3. Rappaport TS, et al. Millimeter wave mobile communications for 5G cellular: It will work! IEEE Access. 1:335–349.May.2013

4. Lee, J; Liang, J; Park, J-J; Kim, M-D. Directional path loss characteristics of large indoor environments with 28 GHz measurements. Proc. IEEE 26th Annu. Int. Symp. Pers., Indoor, Mobile Radio Commun; Aug-Sep. 2015 2204–2208.
5. Lei, M; Zhang, J; Lei, T; Du, D. 28-GHz indoor channel measurements and analysis of propagation characteristics. Proc. IEEE 25th Annu. Int. Symp. Pers., Indoor, Mobile Radio Commun; Sep. 2014; 208–212.
6. Koymen, OH; Partyka, A; Subramanian, S; Li, J. Indoor mm-Wave channel measurements: Comparative study of 2.9 GHz and 29 GHz. Proc. IEEE Global Commun. Conf; Dec. 2015; 1–6.
7. Beauvarlet D, Virga KL. Measured characteristics of 30-GHz indoor propagation channels with low-profile directional antennas. IEEE Antennas Wireless Propag Lett. 1(1):87–90.Feb; 2005
8. Zhu J, Wang H, Hong W. Large-scale fading characteristics of indoor channel at 45-GHz band. IEEE Antennas Wireless Propag Lett. 14:735–738.Dec.2014
9. Moraitis N, Constantinou P. Indoor channel measurements and characterization at 60 GHz for wireless local area network applications. IEEE Trans Antennas Propag. 52(12):3180–3189.Dec; 2004
10. Geng S, Kivinen J, Zhao X, Vainikainen P. Millimeter-wave propagation channel characterization for short-range wireless communications. IEEE Trans Veh Technol. 58(1):3–13.Jan; 2009
11. Jung, M-W; Kim, J; Yoon, Y-K. Measurements of path loss in MM-wave for indoor environments. Proc. IEEE Asia Pacific Microw. Conf; Dec. 2009; 1068–1071.
12. Peter, M; Keusgen, W. Analysis and comparison of indoor wideband radio channels at 5 and 60 GHz. Proc. IEEE 3rd Eur. Conf. Antennas Propag; Mar. 2009; 3830–3834.
13. Abdullah, NF; , et al. Path-loss and throughput prediction of IEEE 802.11ad systems. Proc. IEEE 81st Veh. Technol. Conf; May 2015; 1–5.
14. Kyro M, et al. Measurement based path loss and delay spread modeling in hospital environments at 60 GHz. IEEE Trans Wireless Commun. 10(8):2423–2427.Aug; 2011
15. Zaaimia MZ, Touhami R, Talbi L, Nedil M, Yagoub MCE. 60-GHz statistical channel characterization for wireless data centers. IEEE Antennas Wireless Propag Lett. 15:976–979.Oct. 2015
16. Haneda K, Järveläinen J, Karttunen A, Kyrö M, Putkonen J. A statistical spatio-temporal radio channel model for large indoor environments at 60 and 70 GHz. IEEE Trans Antennas Propag. 63(6):2694–2704.Jun; 2015
17. Jacob, M; Kurner, T. Radio channel characteristics for broadband WLAN/WPAN applications between 67 and 110 GHz. Proc. IEEE Eur. Conf. Antennas Propag; Mar. 2009; 2663–2667.
18. Kajiwara, A. Indoor propagation measurements at 94 GHz. Proc. 6th IEEE Int. Symp. Pers., Indoor, Mobile Radio Commun. Conf; Sep. 1995; 1026
19. Helminger, J; Detlefsen, J; Groll, H. Propagation properties of an indoor-channel at 94 GHz. Proc. Int. Conf. Microw. Millim. Wave Technol; Aug. 1998; 9–14.
20. Maccartney GR, Rappaport TS, Sun S, Deng S. Indoor office wideband millimeter-wave propagation measurements and channel models at 28 and 73 GHz for ultra-dense 5G wireless networks. IEEE Access. 3:2388–2424.Oct.2015
21. Study on Channel Model for Frequency Spectrum Above 6 GHz. 3GPP; Dec, 2016 document TR 38.900
22. Aalto University et al. 5G channel model for bands up to 100 GHz. presented at the 3rd Workshop Mobile Commun. Higher Freq. Bands (MCHFB); Dec. 2016; [Online]. Available: http://www.5gworkshops.com/5GCM.html
23. Rappaport, TS, Heath, RW, , JrDaniels, RC, Murdock, JN. Millimeter Wave Wireless Communications. Englewood Cliffs, NJ, USA: Prentice-Hall; 2015.
24. Deng, S; MacCartney, GR; Rappaport, TS. Indoor and outdoor 5G diffraction measurements and models at 10, 20, and 26 GHz. Proc. IEEE Global Commun. Conf; Dec. 2016; 1–7.
25. Papazian PB, Gentile C, Remley KA, Senic J, Golmie N. A radio channel sounder for mobile millimeter-wave communications: System implementation and measurement assessment. IEEE Trans Microw Theory Techn. 64(9):2924–2932.Sep; 2016

26. Papazian, PB; , et al. Calibration of millimeter-wave channel sounders for super-resolution multipath component extraction. Proc. 10th Eur. Conf. Antennas Propag; Apr. 2016; 1–5.
27. Hausmair, K; Witrisal, K; Meissner, P; Steiner, C; Kail, G. SAGE algorithm for UWB channel parameter estimation. Proc. COST 2100 Manage. Committee Meet; Feb. 2010; 1–7.
28. Gustafson, C; Tufvesson, F; Wyne, S; Haneda, K; Molisch, AF. Directional analysis of measured 60 GHz indoor radio channels using SAGE. Proc. IEEE Veh. Technol. Conf; May 2011; 1–5.
29. Choi, M-S; Grosskopf, G; Rohde, D. Statistical characteristics of 60 GHz wideband indoor propagation channel. Proc. IEEE 16th Int. Symp. Pers., Indoor, Mobile Radio Commun; Sep. 2005; 1–5.
30. Sun, S; MacCartney, GR; Samimi, MK; Rappaport, TS. Synthesizing omnidirectional antenna patterns, received power and path loss from directional antennas for 5G millimeter-wave communications. Proc. IEEE Global Commun. Conf; Dec. 2015; 1–7.
31. Friis HT. A note on a simple transmission formula. Proc IRE. 34(5):254–256.May; 1946
32. Rappaport, TS. Wireless Communications: Principles and Practice. 2. Upper Saddle River, NJ, USA: Prentice-Hall; 2002.
33. Haneda, K; , et al. Indoor 5G 3GPP-like channel models for office and shopping mall environments. Proc. IEEE Conf. Commun; Jul. 2016; 694–699.
34. Hur S, et al. Proposal on millimeter-wave channel modeling for 5G cellular system. IEEE J Sel Topics Signal Process. 10(3):454–469.Apr; 2016
35. Molisch, AF; Karttunen, A; Hur, S; Park, J; Zhang, J. Spatially consistent pathloss modeling for millimeter-wave channels in urban environments. Proc. 10th Eur. Conf. Antennas Propag; Apr. 2016; 1–5.
36. Langen, B; Lober, G; Herzig, W. Reflection and transmission behavior of building materials at 60 GHz. Proc. IEEE Symp. Pers., Indoor, Mobile Radio Commun; Sep. 1994; 505–509.
37. Lee, WCY. Mobile Communications Engineering. New York, NY, USA: McGraw-Hill; 1985.
38. Matolak DW, Remley KA, Gentile C, Holloway CL, Wu Q, Zhang Q. Peer-to-peer urban channel characteristics for two publicsafety frequency bands. IEEE Antennas Propag Mag. 56(5):101–115.Oct; 2014
39. [Accessed on Jul. 2015] 5G mmWave Channel Model Alliance. [Online]. Available: https://www.nist.gov/ctl/5g-mmwave-channel-model-alliance

Biographies

Jelena Senic received the B.S. and M.S. degrees in electrical engineering with a specialization in radiocommunications and information technologies from the School of Electrical Engineering, University of Belgrade, Belgrade, Serbia, in 2009 and 2010, respectively.

Since 2015, she has been a Guest Researcher at the Communications Technology Laboratory, National Institute of Standards and Technology, Boulder, CO, USA. Her current research interests include millimeter-wave communications, measurements of signal propagation, and channel modeling for 5G wireless networks.

Mrs. Senic and her team received the Best Measurement Paper Award in the 11th European Conference on Antennas and Propagation (EuCAP2017), Paris, France.

Camillo Gentile (M'01) received the B.S. and M.S. degrees from Drexel University, Philadelphia, PA, USA, in 1996, and the Ph.D. degree in electrical engineering from Penn State University, State College, PA, USA, in 2001.

His doctoral work focused on computer vision and neural networks. He was involved in mobile *ad hoc* network routing and geolocation systems. Since 2001, he has been a Researcher at the National Institute of Standards and Technology, Gaithersburg, MD, USA. His current interests include public safety communications, radio frequency channel modeling, and 5G networks.

Peter B. Papazian (M'90–SM'98) received the B.S. degree in physics from Stony Brook University, The State University of New York, Stony Brook, NY, USA, in 1973, and the M.S. degree from the Colorado School of Mines, Golden, CO, USA, in 1979.

He was with the Institute for Telecommunications Science, U.S. Department of Commerce, Boulder, CO, USA. He currently conducts propagation research with the Communications Technology Laboratory, National Institute of Standards and Technology, Boulder. He focused on the design of radiowave propagation measurement equipment, field measurement programs, and model development. His current research interests include millimeter-wave wireless communication systems.

Kate A. Remley (S'92–M'99–SM'06–F'13) was born in Ann Arbor, MI, USA. She received the Ph.D. degree in electrical and computer engineering from Oregon State University, Corvallis, OR, USA, in 1999.

From 1983 to 1992, she was a Broadcast Engineer in Eugene, OR, USA, serving as a Chief Engineer of an AM/FM broadcast station from 1989 to 1991. In 1999, she joined the RF Technology Division, National Institute of Standards and Technology, Boulder, CO, USA, as an Electronics Engineer. She is currently the Leader of the Metrology for Wireless Systems Group with NIST. Her current research interests include the development of calibrated measurements for microwave and millimeter-wave wireless systems, the characterization of the link between nonlinear circuits and system performance, and the development of standardized test methods for the wireless industry.

Dr. Remley is a member of the Oregon State University Academy of Distinguished Engineers. She was a recipient of the Department of Commerce Bronze and Silver Medals and an ARFTG Best Paper Award. She was the Chair of the MTT-11 Technical Committee on Microwave Measurements from 2008 to 2010 and the Editor-in-Chief of the IEEE Microwave Magazine from 2009 to 2011, and is the Chair of the MTT Fellow Evaluating Committee. She is a Distinguished Lecturer of the IEEE Electromagnetic Compatibility Society from 2016 to 2017.

Jae-Kark Choi received the B.S. degree in electronic engineering and the M.S. and Ph.D. degrees in information and telecommunication engineering from Inha University, Incheon, South Korea, in 2006, 2008, and 2013, respectively.

From 2013 to 2017, he was a Guest Researcher at the National Institute of Standards and Technology, Gaithersburg, MD, USA. Since 2017, he has been a Senior Engineer at Hanwha Systems R&D Center, Gyeonggi-do, South Korea. His current research interests include millimeter wave, cognitive radio networks, and tactical communications system.

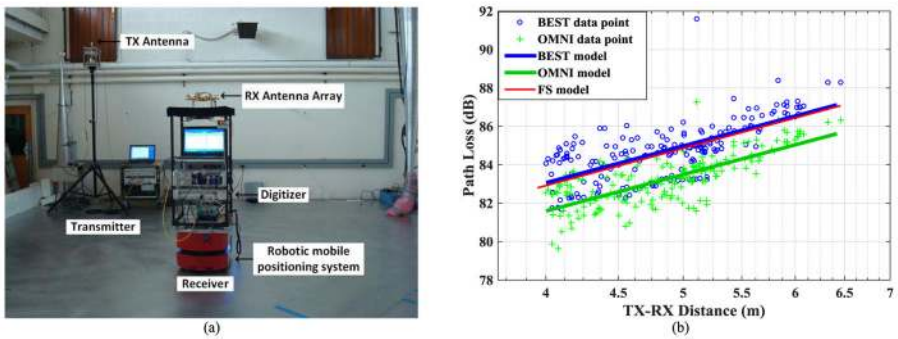

Fig. 1.

(a) mmWave channel sounder in the Basement environment: TX antenna is mounted on the tripod and the RX antenna array is placed on the robot. (b) BEST and OMNI path-loss models based on 351 unique TX–RX configurations in LOS conditions.

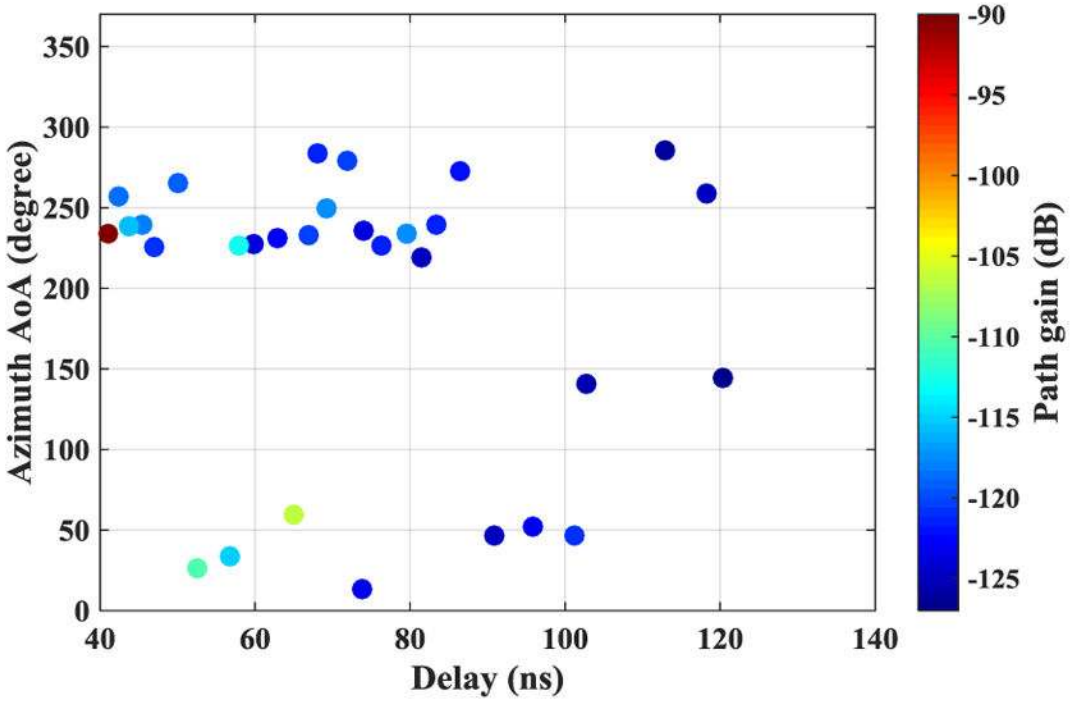

Fig. 2.

Directional CIR of an example TX–RX configuration. Each circle indicates an extracted multipath-channel component color-coded according to the path gain.

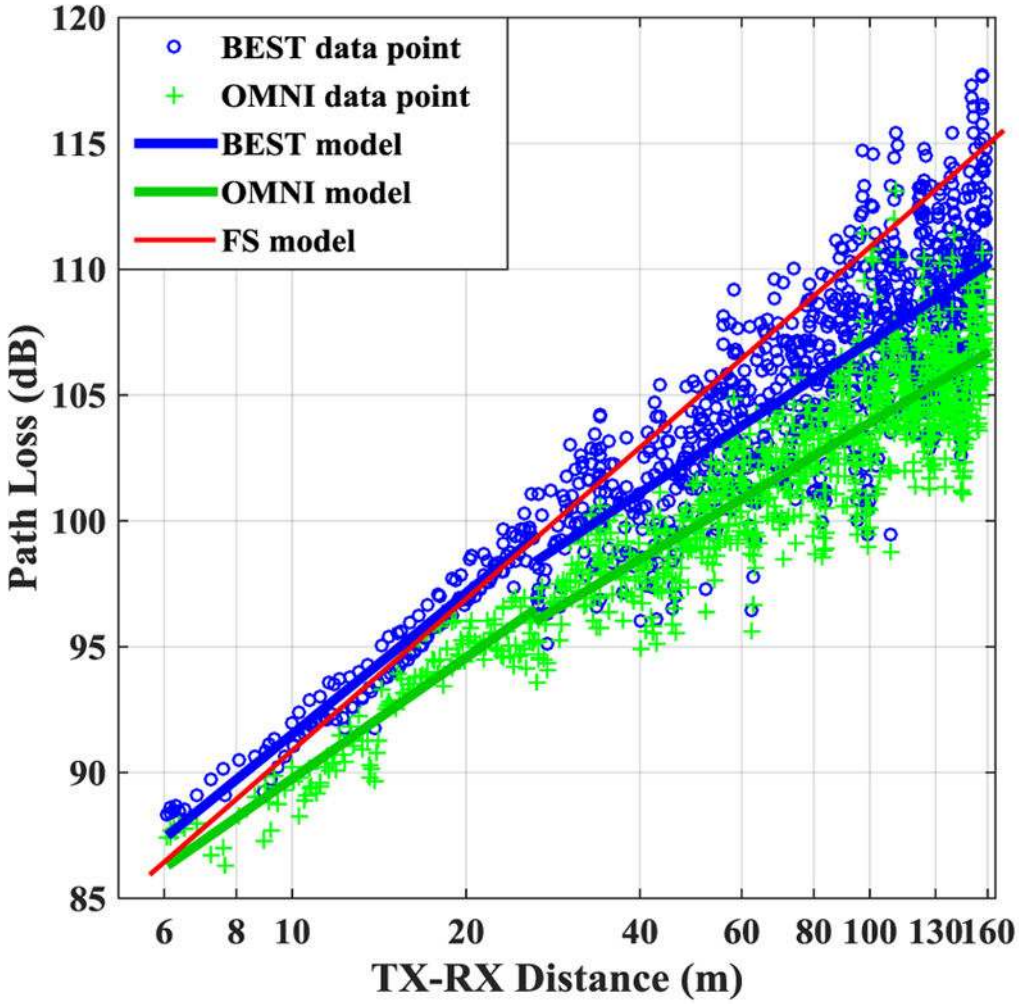

Fig. 3.

Hallway path-loss model. Although RX was in LOS conditions, BP was set at $d_1 = 26.3$ m where discontinuity in the data points caused by staircase started.

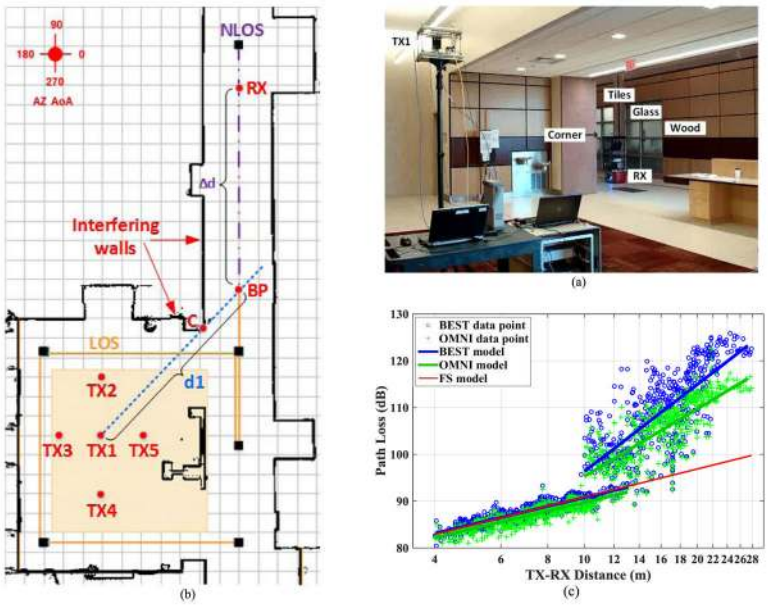

Fig. 4.

Lobby/hallway environment. (a) TX1 position in a lobby area and RX position in the hallway close to the corner where NLOS conditions start. Notice the various types of the wall materials on the right side of the hallway. (b) Floorplan: RX transitions from LOS (solid orange line) to NLOS (dashed-dotted purple line) at the BP, at which it loses the direct path (dotted blue line) from TX1. Thereafter, the TX–RX distance is the BP distance d_1 plus the incremental distance Δd along the hallway. (c) Floating-BP path-loss models generated by combining the data from the five TX positions.

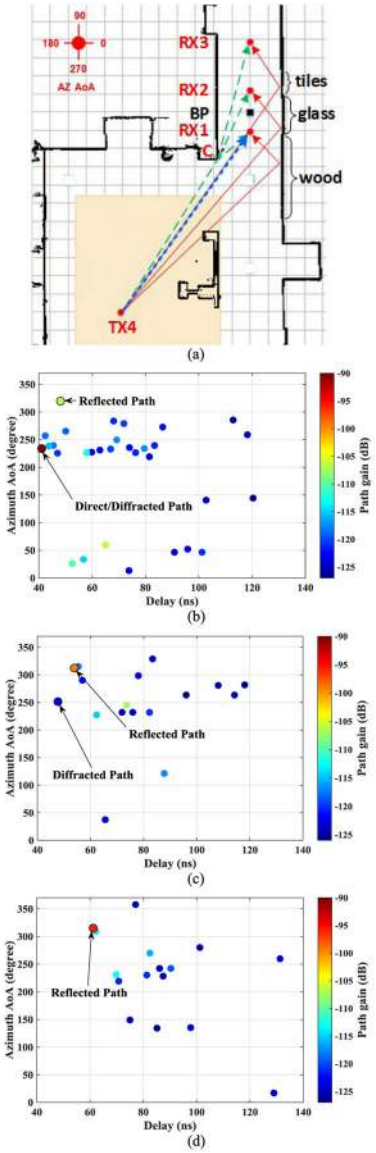

Fig. 5.

(a) Raytracing prediction for three RX positions around the BP of TX4. The propagation mechanisms of direct transmission (blue dots), diffraction (dashed green line), and reflection (solid red line) are depicted at each position. Directional response of (b) RX1, (c) RX2, and (d) RX3.

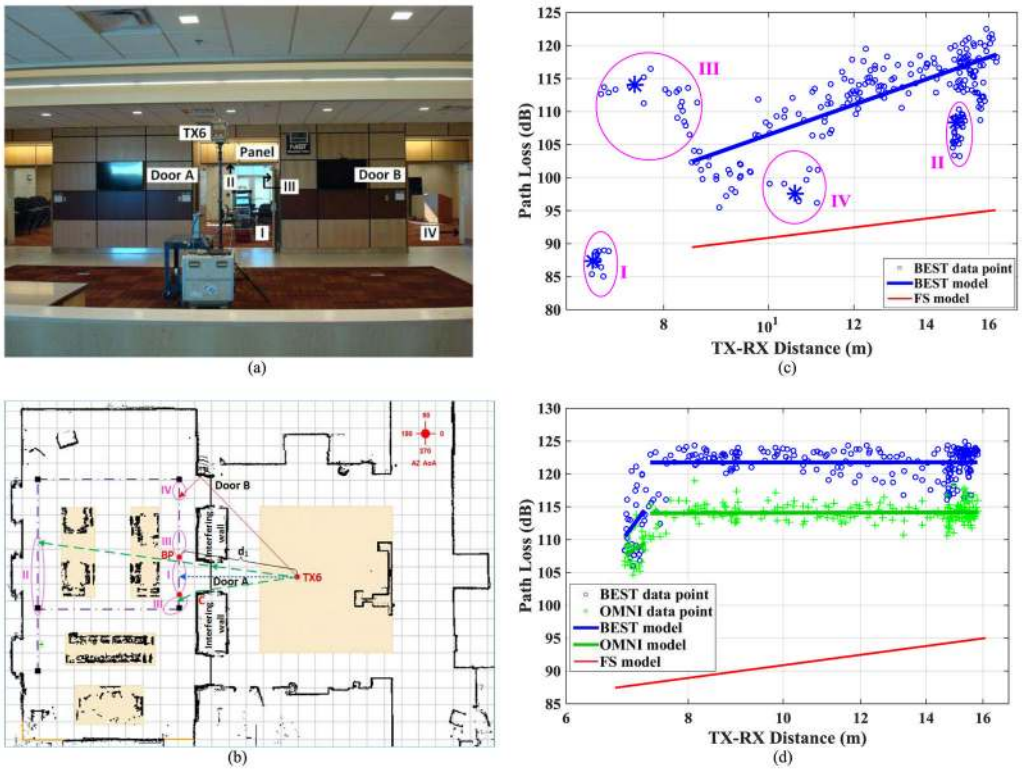

Fig. 6.

(a) Photograph of the lobby/conference room with open doors environment. (b) Floorplan: RX moves along dashed-dotted purple line trajectory in conference room, mostly in NLOS except for Zone I in LOS. The dominant propagation mechanism in each of the Zones I–IV is depicted: direct transmission (dotted blue line), diffraction (dashed green line), or reflection (solid red line). In NLOS, the TX–RX distance is the BP distance d_1 from TX6 to BP, plus the incremental distance (not shown) Δd from the BP to the RX. (c) BEST data points and path-loss model for Open Doors environment. (d) BEST and OMNI path-loss models for lobby/conference room with closed doors environment.

TABLE I

Environment Settings and Path-Loss Model Parameters. The Parameters Shaded in Blue (Bold Values) Are Related to the BEST Model and the Ones in Green to the OMNI Model. The Gray-Shaded Parameters Are n/a

Environment	# Data Points	Range (m)	Wall Materials	d_1(m)	α_0	β_0(dB)	σ_0(dB)	α_1	β_1 (dB)	σ_1 (dB)
Basement	351	4.0–6.5	cinderblock		**1.97**	**71.18**	**1.09**			
					1.96	69.80	0.86			
Hallway	1032	6.0–159.0	stone /wood / glass / metal	26.3	**1.87**	**72.87**	**0.71**	**1.51**	**–0.99**	**2.81**
					1.60	73.77	0.98	1.36	–0.47	1.92
Lobby/Hallway TX1	234	4.0–21.4	stone / wood / glass / metal	10.1	**2.37**	**67.87**	**2.34**	**7.45**	**2.66**	**3.87**
					2.39	66.85	1.73	5.30	3.94	2.28
Lobby/Hallway TX2	210	4.0–18.5		7.8	**1.75**	**73.26**	**1.13**	**4.21**	**14.92**	**3.74**
					1.46	74.66	1.22	3.00	12.96	1.92
Lobby/Hallway TX3	296	4.1–22.0		11.3	**1.87**	**72.00**	**1.25**	**6.16**	**8.44**	**3.04**
					1.90	70.41	1.41	5.52	7.09	2.03
Lobby/Hallway TX4	241	4.0 – 24.0		13.3	**2.05**	**70.16**	**1.27**	**4.38**	**4.40**	**5.35**
					2.05	69.34	1.10	4.11	3.48	3.83
Lobby/Hallway TX5	217	5.0–20.6		9.9	**1.57**	**74.49**	**1.19**	**3.35**	**6.10**	**5.08**
					1.68	72.70	1.19	3.00	5.38	3.73
Lobby/Hallway floating	1198	4.0–24.0			**1.93**	**71.51**	**1.52**	**6.19**	**5.54**	**5.82**
					1.90	70.73	1.40	4.81	5.64	4.06
Lobby/Conf. Room Open	262	6.9–16.3	fabric over sheetrock	7.3				**5.75**	**10.54**	**3.20**
								3.63	10.10	2.12
Lobby/Conf. Room Closed	252	6.9–15.8						**0.00**	**33.60**	**2.21**
								0.04	25.90	1.43

TABLE II

Comparison of Estimated and Predicted Multipath-Component Characteristics in Lobby/Hallway for TX4

Mechanism description	Pied. PL (dB)	Est. PL (dB)	Pred. Delay (ns)	Est. Delay (ns)	Pred. AZ AoA (deg.)	Est. AZ AoA (deg.)
Dir./Diff. at RX1	92.6	90.6	40.6	41.1	234	233.5
Refl. at RX1	94.1	107	48.3	48.2	316.5	319.5
Diff. at RX2	120.1	121.2	46.8	47.8	245.5	251.5
Refl. at RX2	95.0	98.9	53.87	53.87	311	312
Refl. at RX3	96.1	96.0	60.9	61.1	305.5	315

TABLE III

Comparison of Estimated and Predicted Multipath-Component Characteristics in the Lobby/Hallway for TX1–TX5.RX Was in NLOS Conditions Right After BP

	Zone	Pred. PL (dB)	Est. PL (dB)	Pred. Delay (ns)	Est. Delay (ns)	Pred. AZ AoA (deg.)	Est. AZ AoA (deg.)
Reflection	TX1	93.3	103.4	44.28	44.29	323.5	325.5
	TX2	91.9	104.6	37.71	37.76	339.5	346
	TX3	94.3	101.9	49.36	49.36	328	327
	TX4	95.0	98.9	53.87	53.87	311	312
	TX5	92.7	95.5	41.02	41.02	314	314
Diffraction	TX1	119.4	115.6	35.25	34.51	236	235.5
	TX2	120.6	123.2	27	27.66	222	224
	TX3	125.5	124.6	40.1	40.8	234.5	233.5
	TX4	120.1	121.2	46.8	47.8	245.5	251.5
	TX5	109.0	106.5	33.8	34.4	244	249

TABLE IV

Comparison of Distance Metrics in Lobby/Hallway at the NLOS Waypoint at the End of the Hallway

Transmitter	Euclidean distance, d (m)	Piecewise distance, $d_1 + \Delta d$ (m)	Incremental distance, Δd (m)	Average BEST path loss, $\overline{PL}^{BEST}$ (dB)
TX1	21.2	22.6	12.5	120.5
TX2	18.4	21.5	13.7	122.1
TX3	22.0	24.3	13.0	120.0
TX4	24.1	24.8	11.5	108.8
TX5	20.6	20.9	11.0	107.1
Pearson's corr. coef.	−0.49	0.01	0.95	

TABLE V

Comparison of Predicted and Estimated MPC Characteristics in Lobby/Conference Room With Open Doors

Zone	Pred. PL (dB)	Est. PL (dB)	Pred. Delay (ns)	Est. Delay (ns)	Pred. AZ AoA (deg.)	Est. AZ AoA (deg.)
I	87.6	87.2	22.87	23.12	1	1.5
II	109.8	108.4	49.63	50.05	352	350
III	118.3	113.8	24.03	24.45	31	41
IV	91.0	97.8	33.95	33.95	46	46